The Astrophysical Journal, 826:54 (12pp), 2016 July 20 doi:10.3847/0004-637X/826/1/54

LEPTONIC AND LEPTO-HADRONIC MODELING OF THE 2010 NOVEMBER FLARE FROM 3C 454.3

C. Diltz[1] and M. Böttcher[1,2]
[1] Astrophysical Institute, Department of Physics and Astronomy, Ohio University, Athens, OH 45701, USA
[2] Centre for Space Research, North-West University, Potchefstroom, 2520, South Africa
Received 2015 November 5; revised 2016 May 10; accepted 2016 May 15; published 2016 July 20

ABSTRACT

In this study, we use a one-zone leptonic and a lepto-hadronic model to investigate the multi-wavelength emission and prominent flare of the flat spectrum radio quasar 3C 454.3 in 2010 November. We perform a parameter study with both models to obtain broadband fits to the spectral energy distribution (SED) of 3C 454.3. Starting with the baseline parameters obtained from the fits, we then investigate different flaring scenarios for both models to explain an extreme outburst and spectral hardening of 3C 454.3 that occurred in 2010 November. We find that the one-zone lepto-hadronic model can successfully explain both the broadband multi-wavelength SED and light curves in the optical R, *Swift* X-Ray Telescope, and *Fermi* γ-ray band passes for 3C 454.3 during quiescence and the peak of the 2010 November flare. We also find that the one-zone leptonic model produces poor fits to the broadband spectra in the X-ray and high-energy γ-ray band passes for the 2010 November flare.

Key words: galaxies: active – galaxies: jets – gamma rays: galaxies – radiation mechanisms: non-thermal – relativistic processes

1. INTRODUCTION

1.1. Blazars

Blazars are a subclass of radio-loud active galactic nuclei (AGNs) that possess collimated relativistic jets, oriented closely aligned with the line of sight (Schlickeiser 1996; Urry 1998). Blazars are characterized by their highly collimated jets, Doppler boosting, and multi-wavelength variability, in some extreme cases down to a few minutes (Aharonian et al. 2007; Albert et al. 2007). The broadband, multi-wavelength emission of blazars can be characterized by non-thermal continuum spectra with a broad low-frequency component in the radio-UV or even the X-ray range and a high-frequency component that extends from X-rays to high-energy γ-rays. In blazar modeling, it is generally accepted that the low-frequency component is interpreted as synchrotron emission from a distribution of non-thermal electrons in the magnetic field of the jet. The origin of the second, high-frequency component is less clear. Two model paradigms are used in order to explain its origin. These two fundamentally different approaches are referred to as leptonic and hadronic models. For a detailed review, see Böttcher et al. (2012).

In the leptonic model for blazars, the broadband radiation is due mainly to leptons (electrons and positrons), while protons make little to no contribution since they are not accelerated to sufficient energies to produce comparable radiative output. The high-frequency component of the spectral energy distribution (SED) is caused by the inverse Compton scattering of photons in the emission region with non-thermal electrons. Several different seed photon fields can be upscattered by the electrons to produce the broadband emission. These seed photon fields can include the synchrotron emission from the electrons themselves. This process is referred to as synchrotron self-Compton (SSC; Jones 1968). The seed photon fields can also include external photon fields, in a process known as external Compton scattering (EC). Different external photon fields, such as an accretion disk (Dermer et al. 1992; Dermer & Schlickeiser 1993), a broad-line region (BLR; Sikora et al. 1994; Blandford & Levinson 1995), or the dusty (infrared emitting) torus (Blazejowski et al. 2000) surrounding the central accretion flow can serve as target photons that are then upscattered to high-energy γ-rays. The leptonic model of blazar emission has had success in modeling the broadband emission of many blazars.

In the hadronic model of blazars, synchrotron radiation from protons as well as photo-pion-production-induced radiation is responsible for the emission of X-rays to high-energy γ-rays (Mastichiadis & Kirk 1995, 2005). One-zone hadronic models have been used to reproduce the SEDs of both FSRQs and BL Lac objects (e.g., Mannheim & Biermann 1992; Mannheim 1993; Mücke & Protheroe 2001; Yan & Zhang 2014; Cerruti et al. 2015; Petropoulou et al. 2015). Large magnetic fields are often necessary to produce strong synchrotron emission and to ensure that the proton Larmor radius is confined within the size of the emission region. Electron and proton synchrotron radiation represent the main target photon fields through which photo-hadronic interactions can take place, producing charged and neutral pions. The neutral pions decay to produce photons, while the charged pions decay to produce muons and muon neutrinos. The muons then subsequentally decay to produce electrons, positrons, and electron and muon neutrinos. Typically, the synchrotron emission from the intermediate particles is neglected and only the final decay products of the photo-hadronic interactions are considered (Kelner & Aharonian 2008). However, if the magnetic field of the emission region is large enough and the protons carry enough energy, then the synchrotron cooling timescale of the intermediate particles (muons and pions) can be shorter than their decay timescale and synchrotron emission from muons and pions can no longer be neglected (Böttcher et al. 2013). Recently, a time-dependent, one-zone lepto-hadronic model, which includes synchrotron emission from both muons and pions, was used to reproduce the broadband SED of the flat spectrum radio quasar (FSRQ) 3C 279 (Diltz et al. 2015). The emission of muon and pion synchrotron radiation at very high-energy (VHE) γ-rays represents a distinguishing characteristic between leptonic and

hadronic models (Aharonian 2000; Mücke et al. 2003; Sol et al. 2013).

Both one-zone leptonic and hadronic models have been successful to reproduce the SEDs of blazars (e.g., Collmar et al. 2010; Cao & Wang 2014). Therefore, additional diagnostics are needed in order to determine which model is best suited to reproduce all features observed in blazars. One of the more distinct signatures for the hadronic origin of γ-rays is the production of TeV–PeV neutrinos by photo-hadronic interactions. Blazars as sources of high-energy neutrinos have been explored in a number of different studies (Halzen & Zas 1997; Mücke et al. 2003; Dermer et al. 2014; Kistler et al. 2014; Murase et al. 2014). Petropoulou et al. (2015) modeled the broadband SEDs of six BL Lac objects using a one-zone lepto-hadronic model in order to determine the neutrino fluxes from each source. Studies have also been done to determine how the neutrino emission of FSRQs and BL Lac objects contributes to the cosmic neutrino background (Dermer et al. 2014; Murase et al. 2014; Padovani et al. 2015). Detecting neutrino flares during flaring events in different wavelength bands would represent a distinguishing signature for the hadronic origin of the γ-ray emission of blazars. Another unique characteristic that can separate the leptonic and lepto-hadronic origin of γ-ray emission would be the detection of a high degree of polarization from the X-rays and high-energy γ-rays in blazar emission (Zhang & Böttcher 2013; Zhang et al. 2014).

An additional diagnostic that can separate the leptonic and hadronic origin of blazar emission lies in the light curve behavior in different wavelength bands during flaring events. One-zone, time-dependent leptonic models have been used to investigate the flaring behavior of different blazars, such as 1ES 1011+496 (Weidinger & Spanier 2015), Mrk 421 (Asano et al. 2013; Asano & Hayashida 2015), and PKS 0208-517 (Chen et al. 2013). The physical conditions in the jet of a blazar, such as the magnetic field, particle energy, and acceleration efficiency, can be enhanced during a flaring event (Diltz et al. 2015). Following changes in these physical conditions during a flare, particles (electrons/protons) are accelerated and lose energy on different timescales. This, in turn, produces substantially different variability patterns in different wavelength bands for both models. Comparing the light curves in selected bands between both models can help diagnose which model is best suited to explain all spectral and light curve features.

1.2. Observations of 3C 454.3

The FSRQ 3C 454.3 ($z = 0.859$) is one of the brightest and most variable γ-ray sources in the night sky. 3C 454.3 exhibited many outbursts in the pre-*Fermi* era. In 2005, 3C 454.3 displayed a prominent optical outburst, reaching its historical maximum with $R = 12.0$ (Villata et al. 2006). The event triggered follow-up X-ray observations with *INTEGRAL* (Pian et al. 2006) and *Swift* (Giommi et al. 2006), γ-ray observations with AGILE (Vercellone et al. 2007), as well in the radio band, where an outburst with about a one-year delay (Villata et al. 2007) was seen. Since the launch of *Fermi* in 2008 June, 3C 454.3 has exhibited many large bursts in γ-rays and across the entire electromagnetic spectrum. 3C 454.3 displayed prominent outbursts in late 2009, 2010 April, and late 2010 (Ackermann et al. 2010; Bonnoli et al. 2011; Raiteri et al. 2011; Wehrle et al. 2012). In 2010 October, observers noticed that 3C 454.3 was undergoing a pronounced flaring at near-IR wavelengths (Carasco et al. 2010). The flaring was followed up in the optical, UV, X-ray, and γ-ray bands (Vercellone et al. 2011). In the following month, 3C 454.3 obtained its highest flux in γ-rays, peaking around November 19–20 (Sanchez et al. 2010; Striani et al. 2010; Abdo et al. 2011). During this period, 3C 454.3 was extensively monitored in the radio, IR, optical, and X-ray bands. Observations before the main γ-ray flare showed an increase in the form of a plateau, days before the main γ-ray flare occurred (Vittorini et al. 2014). However, cross correlation analysis of the flares in the *Fermi* γ-ray band and the *Herschel*/submillimeter band during the 2010 November flare show no delays between them (Wehrle et al. 2012). The excellent multi-wavelength coverage of this flaring event allows for a careful analysis to understand the conditions of the emission site and the physical mechanism responsible for the flare.

In this paper, we use the codes detailed in Diltz & Böttcher (2014) and Diltz et al. (2015) to provide leptonic and lepto-hadronic fits to the SED of the FSRQ 3C 454.3 to obtain a baseline parameter set. We then choose a subset of parameters from the baseline set and model them as Gaussian perturbations in time in order to simulate the flare that occurred on 2010 November 19–20. We compare the broadband SED of 3C 454.3 during the peak of the flare using both models. Once one model has successfully reproduced the SED during the peak of the flare, we produce flux light curves in the optical R, X-ray, and *Fermi* γ-ray bands. We study the variability patterns and compare the results to the data to discern which model is best suited to explain the SED of 3C 454.3 and the light curves during and the 2010 November flare (Wehrle et al. 2012). We describe the leptonic and lepto-hadronic model setup in Section 2; we present leptonic and lepto-hadronic model fits to the quiescent state SED using the equilibrium solutions to both codes in Section 3; we then investigate the light curves resulting from the Gaussian perturbations of the parameter sets in Section 4; we then discuss the implications of our fits and conclude in Section 5. Throughout this paper, we convert redshift to luminosity distance using a ΛCDM cosmology with $H_0 = 70\ \mathrm{km\ s^{-1}}$, $\Omega_m = 0.3$, $\Omega_\Lambda = 0.7$, giving $d_L = 5.57$ Gpc for 3C 454.3.

2. MODEL SETUP

We consider a homogeneous, one-zone model, where a power-law distribution of ultra-relativistic particles, $Q(\gamma, t) = Q_0 \gamma^{-q} H(\gamma; \gamma_{\rm min}, \gamma_{\rm max})$, is continuously injected into a spherical region of size R, moving along the jet with a bulk Lorentz factor Γ, embedded in a homogeneous, randomly oriented magnetic field of strength B. Here, $H(x; a, b)$ is the Heaviside function defined as $H = 1$ if $a \leqslant x \leqslant b$ and $H = 0$ otherwise. The size of the emission region is constrained through the observed variability timescale, $\Delta t_{\rm var}^{\rm obs}$, using the relation $R \leqslant c\Delta t_{\rm var}^{\rm obs}\delta/(1+z)$, where z denotes the redshift to the source. The emission region moves relativistically along the jet axis with Doppler factor $\delta = 1/\Gamma(1 - \beta_\Gamma \cos\theta)$. The emission is Doppler boosted into a viewing angle of size $\theta_{\rm obs} \approx 1/\Gamma$, enhancing the luminosity by a factor of δ^4 and reducing the variability timescale in the comoving frame by a factor of δ^{-1}.

Both models use coupled second order Fokker–Planck equations to track the time evolution of the particle distributions. We assume that the pitch angle scattering timescale is much smaller than the dynamic timescales. As a result, the

particle distributions are isotropic in the comoving frame of the emission region. The Fokker–Planck equations of each particle species, $i = e^{\pm}$, p, $\pi^{\pm}$, $\mu^{\pm}$, is then written:

$$\frac{\partial n_i(\gamma, t)}{\partial t} = \frac{\partial}{\partial \gamma}\left[\frac{\gamma^2}{(a+2)t_{\rm acc}}\frac{\partial n_i(\gamma, t)}{\partial \gamma}\right] - \frac{\partial}{\partial \gamma}(\dot{\gamma} \cdot n_i(\gamma, t)) + Q_i(\gamma, t) - \frac{n_i(\gamma, t)}{t_{\rm esc}} - \frac{n_i(\gamma, t)}{\gamma t_{\rm decay}} - \frac{n_i(\gamma, t)}{t_{\rm exp}}, \quad (1)$$

where $t_{\rm acc}$ denotes the timescale due to stochastic acceleration, $a = v_s^2/v_A^2$ gives the square of the ratio between the shock and the Alfvén wave velocities, $t_{\rm esc}$ denotes the dynamical escape timescale for the particles which we parametrize as a multiple of the light crossing time, $t_{\rm esc} = \eta\, R/c$ where $\eta \geqslant 1$. The value of η is kept as a free parameter. The term $\dot{\gamma}$ represents the total energy loss rate of a given particle. All charged-particle species lose energy through synchrotron emission, with a cooling rate for a charged particle of mass m_i given by the equation:

$$\dot{\gamma}_{\rm syn} = -\frac{c\sigma_T B^2}{6\pi m_e c^2}\left(\frac{m_e}{m_i}\right)^3 \gamma^2, \quad (2)$$

where σ_T is the Thomson cross section. Particles can also lose energy through inverse Compton scattering of synchrotron photons and photons from external sources (Dermer & Schlickeiser 1993). This process is relevant only for electrons/positrons, as it is heavily suppressed for heavier particles (protons, pions and muons). Protons can also lose energy due to photo-pion production and adiabatic processes (see Hümmer et al. 2010; Diltz et al. 2015). With adiabatic losses, protons will be diluted as the emission region expands. As a result, an additional term, $-n_i(\gamma, t)/t_{\rm exp}$, is included in the proton Fokker–Planck equation to account for this. Here, $t_{\rm exp}$, represents the expansion timescale of the emission region (see Pennanen et al. 2014). We neglect the adiabatic losses of electrons/positrons, pions, and muons in our model. Unstable particles, such as charged pions and muons, decay on a given timescale, $t_{\rm decay}$, in their own rest frame. The term, $-n_i(\gamma, t)/\gamma t_{\rm decay}$, in the Fokker–Planck equation represents the loss of the unstable particles due to decay in the laboratory frame of the emission region.

In both models, the particles interact with magnetohydrodynamic (MHD) Alfvén waves in the plasma. If the Doppler-shifted wave frequency is a constant multiple of the particle gyrofrequency in the particle guiding center frame, then a resonant interaction between the particle and the transverse component of the electric field of the MHD wave will occur (Dermer et al. 1996; Becker et al. 2006; Dermer & Menon 2009). The particle will experience either an accelerating or decelerating electric field in the transverse direction of motion over a fraction of the cyclotron period, resulting in an increase or decrease in energy. The accelerating or decelerating electric field causes the particle distributions to diffuse in energy, pushing particles to higher or lower energies in a diffusion pattern. This stochastic acceleration process typically causes the particle distributions to have a pronounced curvature in the energy spectrum (Schlickeiser 1984). The strength of the particle diffusion depends on the spectral index of the MHD turbulence, p. A Kolmogorov, $p = 5/3$, or a Kraichnan, $p = 3/2$, spectrum are most often used to model MHD turbulence. In this study, we restrict the spectral index of the turbulence to $p = 2$ to simulate hard sphere scattering between the MHD waves and the particle spectra. The stochastic acceleration timescale can be expressed as

$$t_{\rm acc} = \frac{2}{\pi}\left(\frac{p}{p-1}\right)\frac{t_{\rm dyn}}{\beta_A^2 \xi_i}\,\gamma^{2-p}, \quad (3)$$

where $t_{\rm dyn}$ represents the dynamical timescale over the region in which turbulence generated (which may be smaller than the entire emission region), β_A represents the Alfvén velocity of the plasma normalized to the speed of light and ξ_i represents the ratio of the magnetic field fluctuations relative to the background magnetic field, $\xi_i = |\Delta B/B|^2$. The stochastic acceleration timescale is independent of particle mass and will therefore be the same for all charged-particle species (protons, electrons/positrons, pions, and muons). The diffusion term in Equation (1) describes the stochastic acceleration of particles in the quasi-linear approximation (Dermer et al. 1996). For gyro-resonant interactions to occur in the quasi-linear regime, the magnetic field fluctuations must be much smaller than the background magnetic field, $\xi_i \ll 1$. If the energy density in the plasma waves starts to approach the energy density of the magnetic field, then the field becomes disordered and there exists no well defined gyrofrequency. In both models, we use a ratio between the acceleration timescale and the escape timescale as an input parameter. The ratio between the acceleration and escape timescales constrain the maximum size in which turbulence is injected for stochastic acceleration to occur in the quasi-linear regime; see Section 5.

We numerically compute the solution of the Fokker–Planck equation between continuous injection and escape to reproduce the SED fit using the implicit Cranck–Nichelson (CN) scheme. Given the unconditional stability of the CN scheme, we can set the time step to any size. Therefore, to ensure quick convergence to the equilibrium solution of the Fokker–Planck equation, we set the size of the time step in our code initially to $\approx 10^7$ s. This time step size is considerably larger than the timescales for the loss terms, acceleration, and escape terms in all particle Fokker–Planck equations. However, while choosing an arbitrarily large time step allows quick convergence to the equilibrium solution, it fails to probe the evolutionary processes of the particle spectra that can occur on much smaller timescales, such as radiative, adiabatic cooling, and acceleration processes. The Fokker–Planck equations are numerically solved simultaneously with a set of differential equations that track the time evolution of the photon fields until equilibrium is reached.

2.1. Time-dependent Leptonic Blazar Model

The one-zone leptonic model used in this study is based on the work of Diltz & Böttcher (2014). We consider the continuous injection of relativistic electrons into an emission region of size R with a randomly tangled magnetic field of strength B. The electrons emit broadband synchrotron radiation from the radio to UV/soft X-rays. Due to the emission of synchrotron radiation, electrons lose energy at a rate given by Equation (2). Synchrotron emission at lower frequencies starts to becomes more opaque due to synchrotron self absorption,

resulting in a low-energy cutoff below $\approx 10^{11}$–10^{12} Hz. The synchrotron photons created in the emission region can be upscattered through inverse Compton scattering by the same distribution of radiating electrons to produce SSC emission, peaking in the soft X-rays to soft to intermediate γ-rays (Jones 1968).

For FSRQs, a contribution from external Compton scattering is required to provide acceptable SED fits (Ghisellini et al. 1998; Hartman et al. 2001). External radiation fields surrounding the black hole can be upscattered by electrons in the emission region to produce high-energy γ-rays that dominate the overall luminosity of the SED. For the external radiation fields in this study, we consider two sources. The first source is a geometrically thin, optically thick Shakura–Sunyaev accretion disk (Shakura & Sunyaev 1973). The total bolometric luminosity of the accretion disk and the temperature of the innermost stable circular orbit are constrained through the mass of the supermassive black hole and the Eddington ratio of the disk. The second source is a a spherical isotropic blackbody radiation field surrounding the supermassive black hole, resembling a BLR or an infrared dusty torus (Diltz & Böttcher 2014). This approximation has had success in modeling the high-energy γ-ray emission of FSRQs, low-frequency, and intermediate frequency peaked BL Lac objects (Böttcher et al. 2013). Relativistic transformations are then applied to the two external radiation fields in the AGN frame to the comoving frame of the blob. The emission coefficients due to the Compton scattering of the external radiation fields are then evaluated, taking into account the angular distribution of the external photon fields in the comoving frame (Dermer & Schlickeiser 1993; Dermer & Menon 2009). Additional electron/positron pairs can be generated through $\gamma\gamma$ pair production. The electron/positron pairs then give off their own synchrotron radiation and contribute to the optical/UV non-thermal radiation. In our model, we evaluate the pair-production rate of the photon field in the emission region using the expressions provided by Aharonian et al. (1983). In our model, we take into consideration the full Klein–Nishina Compton cross section to evaluate the Compton emission coefficients and the loss rate due to Compton scattering (Dermer & Menon 2009).

2.2. Time-dependent Hadronic Blazar Model

The one-zone lepto-hadronic model considered in this study is based on the work of Diltz et al. (2015). We consider a continuous injection of relativistic electrons and protons into the emission region of size R and magnetic field strength B. Large magnetic fields are necessary for protons to produce significant synchrotron radiation in the broadband SED. High B fields are also needed to ensure that the proton Larmor radius is confined to within the size of the emission region, $R \approx 10^{15}$–10^{16} cm. Following the initial injection, the electrons and protons give off synchrotron radiation from the radio to high-energy γ-rays and lose energy at a rate given by Equation (2). The time evolution of the electrons/positrons and protons are modeled through separate Fokker–Planck equations. The proton Fokker–Planck equation incorporates losses due to synchrotron, pion production, and adiabatic processes; see Equation (1). With the proton distribution and the seed photon fields generated from the synchrotron emission, we evaluate the pion-production rates based on the photo-hadronic interaction cross section between protons and photons. The total proton-photon interaction cross section is divided into separate components, corresponding to different channels through which the neutral and charged pions are produced: resonances (such as the Δ resonance), direct (non-resonant) production and multi-pion production (Hümmer et al. 2010). We assume the target photon field for photo-pion production is isotropic in the emission region. This limits the model to consider only photon fields that are produced in the emission region (synchrotron radiation). Incorporating external photon fields in the pion-production rates would require an additional integration of the differential cross section against the proton and photon angular distributions.

We track the time evolution of the charged pions through a separate Fokker–Planck equation. The pions are subjected to synchrotron losses, escape, and stochastic acceleration. There is an additional loss term in the pion Fokker–Planck equation due to pion decay. The pion decay timescale in the particle rest frame is $t_{\rm decay} \approx 10^{-8}$ s. Because of the short decay time for the neutral pions, $t_{\rm decay} \approx 10^{-17}$ s, we assume the neutral pions decay instantaneously. An injection term is used for a separate muon Fokker–Planck equation from the decay of charged pions. The muons follow their own Fokker–Planck equation, losing energy due to synchrotron losses and gaining energy from stochastic acceleration. The muon decay timescale in the laboratory frame is longer than for charged pions, $t_{\rm decay} \approx 10^{-6}$ s. As a result, charged muons can produce more synchrotron radiation before they decay compared to charged pions. The high-energy protons must meet certain constraints with the magnetic field before pions and muons are energetic enough to produce synchrotron emission before decaying. If the muon and pion synchrotron radiation timescales are shorter than the decay timescale in the comoving frame and the photo-pion losses are comparable to the proton synchrotron losses, then pion and muon synchrotron emission can no longer be neglected (Böttcher et al. 2013). The code of Diltz et al. (2015) allows us to choose arbitrary values of the maximum proton Lorentz factor and magnetic field, including the regime

$$B\gamma_p \geqslant \begin{cases} 7.8 \times 10^{11} & \text{for pions,} \\ 5.6 \times 10^{10} & \text{for muons.} \end{cases} \quad (4)$$

in which muons and pions produce substantial synchrotron emission. Charged muons then decay to produce electron/positron pairs. A loss term in the muon Fokker–Planck equation due to charged muon decay serves as an additional injection term of electrons and positrons. The electrons/positrons generated through pair production, muon decay, and from the original power-law injection represent the source term for the electron/positron Fokker–Planck equation. The four coupled Fokker–Planck equations are solved simultaneously with the differential equations that model the time evolution of the synchrotron photon fields for each particle species: protons, charged pions, charged muons, and electrons/positrons until the systems reach equilibrium. Bethe–Heitler pair production is not expected to play an important role in our model since the pion-production rate dominates over the loss rate from BH pair production, so it is therefore neglected. Inverse Compton scattering is also neglected in our model since the large magnetic field strengths in the emission region make inverse Compton scattering less efficient for all particle species.

3. COMPARATIVE MODELING OF 3C 454.3

In this section, we apply our leptonic and lepto-hadronic models discussed in the previous sections to the broadband SED of the FSRQ 3C 454.3. With the broadband multi-wavelength observations carried out on 3C 454.3 between MJD 54682-54770 (Abdo et al. 2010), a set of input parameters for both models can be constrained. For 3C 454.3, we have the following observational parameters (see Böttcher et al. 2013 for references to the observational data). With the redshift, $z = 0.857$, the luminosity distance to the source can be determined, which sets the overall luminosity scale. Superluminal motions in the jet of 3C 454.3, $\beta_{\perp,\rm app} \approx 15$, places a lower limit on the bulk Lorentz factor, $\Gamma \geqslant 15$. The bulk Lorentz factor constrains the angle of the observer relative to the jet axis, $\theta_{\rm obs} \leqslant 1/\Gamma$. The observed variability timescale, $\Delta t_{\rm var}^{\rm obs} \approx 1$ day, constrains the size of the emission region, $R \leqslant c\Delta t_{\rm var}^{\rm obs}\delta/(1+z)$. The mass of the supermassive black hole, $M_{\rm BH} \approx 2.0 \times 10^9\, M_\odot$ (Bonnoli et al. 2011), and the accretion disk luminosity, $L_{\rm disk} \approx 2.6 \times 10^{46}\,{\rm erg\,s^{-1}}$ (Jorstad et al. 2013), allows the accretion disk spectral component to be determined. The measured luminosity of the BLR, $L_{\rm BLR} \approx 2.5 \times 10^{45}\,{\rm erg\,s^{-1}}$, allows the size of the assumed spherical BLR to be estimated, $R_{\rm BLR} \approx 0.25$ pc (Bentz et al. 2013). We approximate the BLR spectrum as a thermal blackbody with a temperature of $T_{\rm BLR} \approx 6.0 \times 10^4$ K, which peaks in the UV.

From the set of constrained input parameters, we use a "fit-by-eye" method to determine the remaining set of parameters for both models. The unconstrained parameters are adjusted until a reasonable fit is obtained. The spectral shape and normalization of the multi-wavelength emission in different wavelength bands allows the spectral shape and the normalization of the particle distributions to be determined. The magnetic field is also adjusted to provide reasonable fits to the peaks for the synchrotron, SSC, and EC components for the one-zone leptonic model. For the lepto-hadronic model, we require that the proton distribution and the magnetic field are constrained in such a way so that muon and pion synchrotron emission cannot be neglected in the SED fitting. We aim to set the input parameters in such a way that approximate equipartition between the particle energy and the energy density of the magnetic field is achieved for both models. If the relativistic jets of AGNs are powered by the rotational energy of the central black hole, the jet will be initially Poynting-flux-dominated before the magnetic field converts its energy into particle kinetic energy. This conversion is expected to stop at approximate equipartition.

3.1. Leptonic Model Fits

Figure 1 shows the SED of 3C 454.3 and our leptonic model fit. The input parameters used for the leptonic fit are given in Table 1. We find that the leptonic fitting is satisfactory for the quiescent state for the FSRQ 3C 454.3. The IR/optical/UV emission is well explained by synchrotron emission from the electrons/positrons. Magnetic field values of $B \approx 1$ G are needed to produce satisfactory fits for our leptonic model, consistent with previous findings for magnetic field strength for one-zone leptonic models (Finke & Dermer 2010; Böttcher et al. 2013; Dermer et al. 2014). The synchrotron emission becomes opaque at longer wavelengths due to synchrotron self absorption, producing a cutoff below 10^{12} Hz. The observed radio emission seen is due to more extended regions beyond the zone modeled that have had longer time to emit synchrotron radiation. We also find from the fits that the soft to intermediate X-rays are best explained by SSC emission, in accordance with leptonic modeling. While there are no observational features in the SED indicative of a thermal component from the disk, we include the spectral component of the accretion disk for completeness.

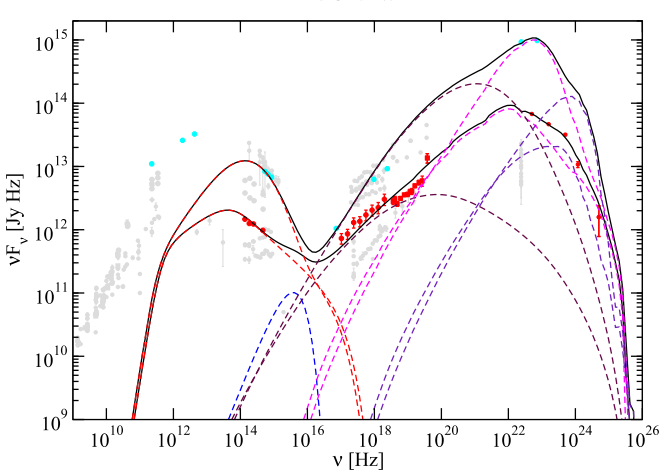

Figure 1. Broadband fit to the SED of 3C 454.3 using our leptonic model during the quiescent and flaring states. The quiescent state data points included in the fit are plotted in red; additional archival data is plotted in gray (data from Abdo et al. 2010). Broadband data during the 2010 November 19–20 flare are plotted in cyan (Wehrle et al. 2012). The model curves are as follows: black solid—total spectrum; red dashed—synchrotron emission from electrons/positrons; maroon dashed—synchrotron self Compton emission; blue dashed—thermal emission from accretion disk; magenta dashed—EC emission from accretion disk; indigo dashed—EC emission from BLR.

From the variability timescale, we can constrain the location of the emission region to be around $R_{\rm axis} = 2\Gamma^2 c\Delta t_{\rm var}^{\rm obs}/(1+z) \approx 0.12$ pc. This places the emission zone within the BLR, located at $R_{\rm BLR} \approx 0.25$ pc. Using the location of the emission region, we compute the external Compton spectral components from the accretion disk and the BLR using the full Compton cross section. We find that an extensive contribution from inverse Compton scattering of the external radiation fields (accretion disk and BLR) is necessary to explain the low to high-energy γ-ray emission in the quiescent state of the blazar 3C 454.3. Below a spectral break centered at 2 GeV, the γ-ray emission is explained by external Compton scattering from the accretion disk, while above the break it is almost entirely from the Compton scattering of the BLR. The combination of the two external Compton components is able to reproduce the spectral break observed at 2 GeV, consistent with previous leptonic modeling of 3C 454.3 (Finke & Dermer 2010; Böttcher et al. 2013). The input parameters imply a accretion disk luminosity of $L_d \approx 10^{46}\,{\rm erg\,s^{-1}}$ and a luminosity of an external radiation field of $L_{\rm BLR} \approx 2.0 \times 10^{45}\,{\rm erg\,s^{-1}}$ to provide a satisfactory fit to the quiescent state SED. These values are in accordance with observations and previous leptonic model fits for 3C 454.3 using a one-zone leptonic model (e.g., Finke & Dermer 2010; Jorstad et al. 2013). Relatively long escape timescales are needed, $t_{\rm esc} \approx 10^7$ s, to ensure that electrons have enough time to cool to produce the low-energy tail of the EC disk component dominating at hard X-rays/soft γ-rays.

With the magnetic field strength and the energy spectrum for the electron distribution, we can compute the magnetization

Table 1
Parameter Values used for the Leptonic and Lepto-hadronic Equilibrium Fit to the Quiescent State SED of 3C 454.3

Parameter	Symbol	Leptonic Value	Hadronic Value
Magnetic field	B	1.5 G	125 G
Radius of emission region	R	2.51×10^{16} cm	2.51×10^{16} cm
Multiple for escape timescale	η	15	15
Bulk Lorentz factor	Γ	15	15
Observing angle	$\theta_{\rm obs}$	6.66×10^{-2} rad	6.66×10^{-2} rad
Proton injection minimum energy	$\gamma_{\rm p,min}$	⋯	1.0
Proton injection maximum energy	$\gamma_{\rm p,max}$	⋯	4.85×10^{8}
Proton injection spectral index	q_p	⋯	2.25
Proton injection luminosity	$L_{\rm p,inj}$	⋯	3.75×10^{46} erg s^{-1}
Electron injection minimum energy	$\gamma_{\rm e,\ min}$	9.0×10^{2}	5.0×10^{1}
Electron injection maximum energy	$\gamma_{\rm e,max}$	6.0×10^{4}	2.5×10^{3}
Electron injection spectral index	q_e	2.9	2.9
Electron injection luminosity	$L_{\rm e,\ inj}$	2.45×10^{43} erg s^{-1}	3.64×10^{42} erg s^{-1}
Supermassive black hole mass	$M_{\rm BH}$	$2.0 \times 10^{9}\ M_{\odot}$	$2.0 \times 10^{9}\ M_{\odot}$
Eddington ratio	$l_{\rm Edd}$	4.0×10^{-1}	4.0×10^{-1}
Accretion disk luminosity	$L_{\rm disk}$	1.0×10^{46} erg s^{-1}	1.0×10^{46} erg s^{-1}
Blob location along the jet axis	$R_{\rm axis}$	0.12 pc	0.12 pc
Radius of broad-line region	$R_{\rm BLR}$	0.25 pc	0.25 pc
Luminosity of broad-line region	$L_{\rm BLR}$	2.0×10^{45} erg s^{-1}	2.0×10^{45} erg s^{-1}
Ratio of ACC and ESC timescales	$t_{\rm acc}/t_{\rm esc}$	0.1	4.0
Luminosity of magnetic field	L_B	1.18×10^{45} erg s^{-1}	7.5×10^{48} erg s^{-1}
Luminosity of electrons	L_e	6.11×10^{45} erg s^{-1}	4.49×10^{42} erg s^{-1}
Ratio of magnetic and electron luminosity	ϵ_{Be}	0.19	1.67×10^{6}

parameter, i.e., the ratio between the luminosities carried in magnetic fields and the electron kinetic energy, for which we find $\epsilon_{Be} = L_B/L_e \approx 10^{-1}$. This result is also consistent with previous findings for 3C 454.3 (e.g., Finke & Dermer 2010).

3.2. Hadronic Model Fits

Figure 2 shows the SED fitting for our lepto-hadronic model used in this study. Table 1 gives the corresponding set of input parameters used for the fitting. We also find reasonable fits for the lepto-hadronic model to the quiescent state of 3C 454.3. The IR/optical/UV emission is again explained by synchrotron emission of electrons/positrons. The electron injection requires low electron injection energies, $\gamma_{e,\rm min} \approx 100$, and soft spectral indices, $q_e \approx 2.9$, to provide satisfactory fits. The soft X-ray to intermediate/hard γ-ray emission is explained by the synchrotron radiation from protons. The spectral fits required ultra-relativistic energies for the protons, around $E_p \sim 10^{17}$ eV to reproduce the γ-ray spectra. The curvature of the proton synchrotron spectrum is able to reproduce the spectral break in the γ-rays observed at ∼2 GeV.

A large magnetic field strength of $B \sim 100$ G is needed in order to produce the necessary proton synchrotron radiation to provide adequate fits to the X-ray to γ-ray broadband emission. The protons then interact with the primary electron and proton synchrotron radiation and, through photo-hadronic interactions, produce pions and muons. With the maximum proton Lorentz factor and magnetic field strength used, the muon synchrotron cooling timescale becomes smaller than the decay timescale in the blob frame. As a result, muon synchrotron radiation becomes non-negligible and produces high-energy γ-rays centered at ∼20 GeV. The combination of proton and muon synchrotron produces a shoulder in the high-energy γ-ray spectrum around 20 GeV; see Figure 2. The charged pions produce their own synchrotron spectral component, but the emission is negligible in comparison to the muon synchrotron

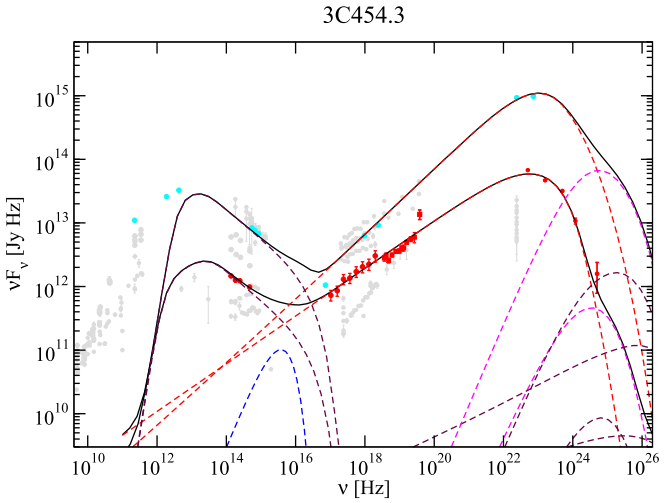

Figure 2. Broadband fit to the SED of 3C 454.3 using our lepto-hadronic model during the quiescent and flaring states. The quiescent state data points included in the fit are plotted in red; additional archival data is plotted in gray (data from Abdo et al. 2010). Broadband data during the 2010 November 19–20 flare are plotted in cyan (Wehrle et al. 2012). The model curves are as follows: black solid—total spectrum; red dashed—proton synchrotron emission; maroon dashed—synchrotron emission from electrons/positron; blue dashed—thermal emission from accretion disk; magenta dashed—pion synchrotron; indigo dashed—pion synchrotron.

emission. The muons subsequently decay and produce electron/positron pairs that generate their own synchrotron spectral component. However, the synchrotron emission from the electron/positrons generated from charged muon decay is also negligible compared to the proton synchrotron.

Using the magnetic field strength and the energy spectrum for the proton distribution, we find a magnetization parameter of $\epsilon_{Bp} = L_B/L_p \approx 1.12$. This result suggests that the emission region is slightly magnetically dominated, suggesting that in an originally Poynting-flux-dominated outflow, magnetic energy

may have been efficiently converted into particle kinetic energy. This result contrasts with the leptonic one-zone fit for 3C 454.3 in which the emission region is more particle-dominated.

4. MODELING THE LIGHT CURVES OF 3C 454.3

The success of both one-zone leptonic and lepto-hadronic models in reproducing the broadband SEDs of blazars makes it difficult to determine the origin of the high-energy γ-ray emission observed. However, blazars exhibit strong flaring across the electromagnetic spectrum, in which the different spectral components change and evolve on different timescales. Blazar flares have often been attributed to the development of strong internal shocks taking place within the jet (Joshi & Böttcher 2011; Saito et al. 2015). The development of a strong shock can have a profound effect on the physical conditions in the jet, accelerating particles to extreme energies. Detailed particle-in-cell (PIC) and MHD simulations have shown that magnetic reconnection can serve as a viable acceleration mechanism to produce non-thermal particles in the downstream region of a strong shock (Hoshino 2012; Sironi & Spitkovski 2014). Magnetic energy dissipation can also be enhanced by increased turbulence produced by strong shocks. Turbulence has been shown to play an important role in the dynamical evolution of magnetic reconnection (Matthaeus & Lamkin 1986; Lazarian & Vishniac 1999; Yokoi et al. 2013). Shock induced turbulence can also play an essential role in the production of non-thermal particles through the stochastic acceleration of particles (Veltri et al. 1998; Greco et al. 2002; Lazarian et al. 2012). These results show close links between the magnetic field, stochastic acceleration timescale, particle injection luminosity, and the particle spectral index during the development of a strong shock. How these spectral components change and the rate at which they change can serve as a diagnostic tool to distinguish which model can best explain both the quiescent and flaring states exhibited by blazars. Starting with the parameter sets of the quiescent state SED fits for 3C 454.3 using the leptonic and lepto-hadronic models, we apply perturbations to a subset of the input parameters of both models in order to reproduce the exceptional flare observed on 2010 November 19–20.

We begin by allowing both models to reach equilibrium for the SED fits of 3C 454.3 as described in the previous section. We then modify the time step to $\Delta t = 2.0 \times 10^6$ s in the comoving frame, corresponding to $\approx 1.3 \times 10^5$ s in the observer's frame. This allows us to resolve light curve patterns on timescales characteristic of synchrotron cooling effects of the relativistic protons and the acceleration timescales for the individual particle distributions. However, we are unable to model shorter-term variability timescales, potentially caused by the synchrotron cooling of high-energy electron-positron pairs generated from the decay of charged mesons, since their cooling timescales are significantly shorter than the size of the time step selected for these simulations. Therefore, we do not explore predicted variability patterns on such short timescales, as this would increase the required computational time significantly.

We choose four input parameters to modify in both models for our light curve analysis: the particle injection luminosity, the particle spectral index, the background magnetic field, and the stochastic acceleration timescale. We modify the perturbations of the selected input parameters in the form of a Gaussian function in time:

$$L_{\mathrm{inj},i}(t) = L_{\mathrm{inj},0,i} + K_{L,i} \cdot e^{-(t-t_0)^2/2\sigma^2}, \quad (5)$$

$$q_i(t) = q_{i,0} + K_{q,i} \cdot e^{-(t-t_0)^2/2\sigma^2}, \quad (6)$$

$$B(t) = B_0 + K_B \cdot e^{-(t-t_0)^2/2\sigma^2}, \quad (7)$$

$$t_{\mathrm{acc}}(t) = \frac{t_{\mathrm{acc},0}}{1 + K_{t_{\mathrm{acc}}} \cdot e^{-(t-t_0)^2/2\sigma^2}}, \quad (8)$$

where the constant K denotes the strength of the perturbation. The terms $L_{\mathrm{inj},0,i}$, $q_{i,\ 0}$, B_0, and $t_{\mathrm{acc},\ 0}$ denote the particle injection luminosity, spectral index, background magnetic field, and stochastic acceleration timescale during quiescence, respectively. The variable σ represents the duration of the perturbation in the comoving frame and t_0 denotes the time where the perturbation peaks in our simulation. In our simulations, we set $t_0 = 5.0\sigma$. This way, for $t = 0$, the perturbed parameter values are essentially identical to their equilibrium values, since $e^{-25} \ll 1$. The value of σ determines the rise times of the light curves. If the cooling timescale in a given bandpass is larger than σ, then the light curve will decay on a timescale of the order of the cooling timescale. If, however, the cooling timescale is smaller, then the decay timescale of the light curve will be of the order σ. No extensive simultaneous SED data was collected during the periods of enhanced activity that occurred both before and after the main flare on November 19–20. Attempting to model the enhanced flux states in the optical R, *Swift* X-Ray Telescope (XRT), and *Fermi* γ-ray bands without SED data would introduce a large number of additional unconstrained parameters, yielding little additional insight into the physical mechanism responsible for the enhanced activity. For this reason, the flare is modeled using the quiescent state as the initial condition; the periods of enhanced activity before and after the flare are neglected.

4.1. Leptonic Model Variability Analysis

We now proceed to the search for a suitable combination of input parameter variations to reproduce both the flare-state SED and the multi-wavelength light curves of 3C 454.3 (see Figure 1). The combination of perturbations has to reproduce similar levels of flux increase in the optical and high-energy γ-ray bands and a much weaker flux increase in the X-ray band. We begin by decreasing the acceleration timescale from its background value to $t_{\mathrm{acc}}(t = t_0) = t_{\mathrm{acc},0}/35$. This decrease is motivated to ensure that the acceleration timescale drops below the cooling timescale for electrons producing synchrotron emission in the optical, $t_{\mathrm{cool}} \approx 10^5$ s in the comoving frame. The decrease in the acceleration timescale causes the electrons to be accelerated to higher energies. As a result, the synchrotron emission, SSC, and external Compton components are shifted to higher energies, and the SSC-dominated X-ray flux drops. Higher energy electrons also produce increased external Compton emission (see Diltz & Böttcher 2014). The decreased acceleration timescale also changes the electron energy distribution, causing the synchrotron emission to display a pronounced curvature in the spectrum. Shifting the electrons to higher energies also causes the spectral components to become narrower since the low-energy tail of the electron energy distribution is disrupted by the acceleration.

Table 2
Model Light Curve Fit Parameters for the Lepto-hadronic Model

Scenario	K_L (erg s^{-1})	K_q	K_B (G)	$K_{t_{acc}}$
Electron (Leptonic)	8.0×10^{44}	⋯	−0.9	34.0
Proton (Lepto-hadronic)	⋯	−0.3	−50.0	3.0
Electron (Lepto-hadronic)	4.5×10^{43}	⋯	−50.0	3.0

Note. Negative value for the perturbation of the particle spectral index indicates spectral hardening. Conversely, a positive value indicates a spectral softening. σ values are taken in the comoving frame.

The optical and high-energy γ-ray emission increases while the X-ray emission subsequently decreases.

To offset the decrease in X-ray emission from altering the acceleration timescale, we increase the electron injection luminosity from $L_{\mathrm{inj},0,e} = 2.5 \times 10^{43}\,\mathrm{erg\,s^{-1}}$ to $L_{\mathrm{inj},e}(t = t_0) = 8.25 \times 10^{44}\,\mathrm{erg\,s^{-1}}$. This subsequently causes all spectral components to increase in flux. The effect is most pronounced in the X-rays since the SSC flux scales as n_e^2. Increasing the electron injection luminosity also causes the non-thermal and thermal particle densities to increase. This, in turn, causes the Alfvén velocity of the plasma to decrease, resulting in decreased diffusion due to stochastic acceleration. The result is that both the electron synchrotron and SSC spectral components reach their peak levels for the SED, but the EC emission from the accretion disk and BLR still underpredicts the flux levels in the γ-ray bandpass. Increasing the electron injection causes the flux levels in the optical R and X-ray to overshoot.

The background magnetic field is then decreased from $B_0 = 1.5\,\mathrm{G}$ to $B(t = t_0) = 0.5\,\mathrm{G}$. Weakening the magnetic field inhibits synchrotron cooling for the highest energy electrons and causes them to be accelerated to even higher energies. A magnetic field decrease can represent a magnetic reconnection event where the magnetic energy is converted into particle kinetic energy. With the lower B field, the synchrotron emission decreases as a result. This, in turn, causes the SSC emission to decrease as well. The higher energy electrons push the external Compton scattering of the accretion disk to higher fluxes and energies. Decreasing the magnetic field any further causes the model to overpredict the *Fermi* γ-ray flux, while at the same time underpredicting the flux in the optical R and *Swift* XRT band passes. From the fits, we find that changing the spectral index of the electron injection is unnecessary. Since the electrons are already heavily accelerated, changing the electron spectral index will only increase the number of high-energy electrons rather than the flux levels in the high-energy γ-ray band.

With the chosen combination of variations of the magnetic field, acceleration timescale and electron injection luminosity (see Table 2), we obtain flux levels that are in rough agreement with the flare-state SED of 3C 454.3. However, the spectral fits in the X-ray and high-energy γ-rays are inconsistent with the observations. While, due to the decreased acceleration timescale, the SSC and EC components shift to higher energies, the decreased number of low-energy electrons depletes the low-energy SSC and EC photons, generating poor spectral fits to the X-ray and high-energy γ-ray bands during the peak of the flare. A high acceleration efficiency is necessary to upscatter photons from external sources to the flux levels of the 2010 November flare. Reducing the acceleration efficiency would improve the fits to the X-ray spectra, but it then underpredicts the flux levels

FERMI Flare (Nov 2010):

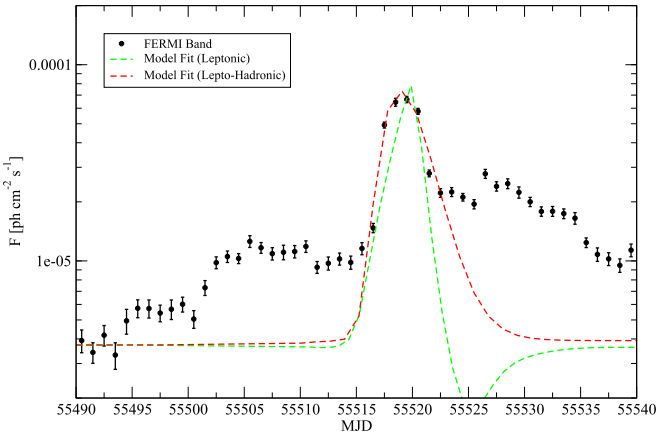

Figure 3. Light curve fit between the data (Wehrle et al. 2012) of the 2010 November 19–20 (MJD 55519-55520) flare and the leptonic and lepto-hadronic models in the *FERMI* bandpass (20–300) GeV in units of ph cm^{-2} s^{-1}.

Swift XRT Flare (Nov 2010):

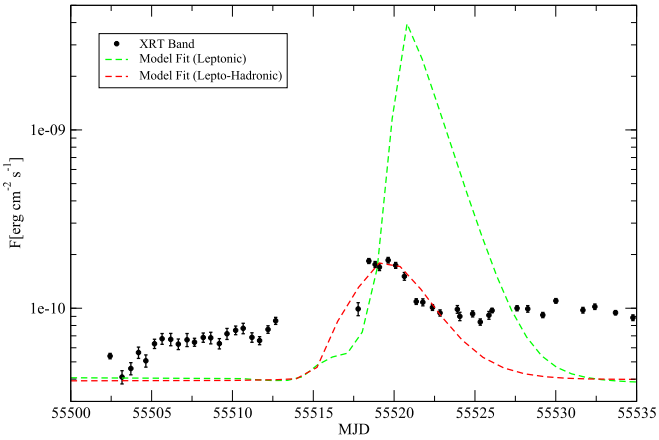

Figure 4. Light curve fit between data of the 2010 November 19–20 (MJD 55519-55520) flare and the leptonic and lepto-hadronic models in the *Swift* XRT bandpass (0.2–10) keV in units of erg cm^{-2} s^{-1}.

in the high-energy γ-ray band during the peak of the flare. A reduced magnetic field is also necessary since weaker synchrotron cooling produces even more energetic electrons to upscatter the photons in the emission region. Increasing the magnetic field produces stronger cooling and less high-energy electrons, inhibiting Compton scattering processes. The reduced synchrotron emission in the IR/optical/UV is then offset by a larger electron injection luminosity. Once the perturbations have subsided, the electrons rapidly cool by synchrotron and Compton processes. The rapid cooling produces a sharp drop in the high-energy electrons responsible for the optical R and high-energy γ-ray emission; see Figures 3 and 5. The electrons pile up at lower energies, producing a major flare in X-rays before finally returning to the pre flux levels; see Figure 4. The strength of the perturbations used in the SED fits for our one-zone leptonic model is given in Table 2. The resultant fits to the SED during the peak of the flare is given in Figure 1. Based on these considerations, we conclude that the one-zone leptonic model cannot reproduce the SED during the peak of the 2010 November flare.

4.2. Hadronic Model Variability Analysis

In a one-zone lepto-hadronic model, different particle distributions produce the non-thermal emission in different band passes. Changing any one of the four originally selected input parameters produces different effects to the individual particle distributions in comparison to the leptonic model. Following the same procedure as our one-zone leptonic model, we decrease the stochastic acceleration timescale to $t_{\rm acc}\,(t = t_0) = t_{\rm acc,0}/4$. This acceleration timescale change applies to all particle distributions (see Equation (1)). Since the magnetic field is much higher and the diffusion coefficient (responsible for stochastic acceleration) is larger, a modest change to the acceleration timescale is needed to accelerate protons to larger energies in comparison to the leptonic model. Decreasing the acceleration timescale causes low-energy protons to pile up at higher energies, producing flares in the X-ray and high-energy γ- ray bands. The higher energy protons interact with the increased proton synchrotron photon field and produce more energetic pions and muons, which then decay to produce high-energy electrons/positrons. The increased amount of synchrotron radiation from both the muons and pions produces a major VHE γ-ray flare beyond 20 GeV. Unfortunately, no observations were carried out with HESS or MAGIC that could have potentially detected flaring activity in the VHE γ-ray band. Altering the stochastic acceleration timescale produces no effect on the electron distribution responsible for the optical emission. This is due to the large magnetic field present in the emission region and the extremely short electron cooling timescales that dominate the evolution of the particle distribution in the Fokker–Planck equation. This signature is unique to lepto-hadronic models in that an X-ray and γ-ray flare can present itself while leaving the optical emission unaffected by simply changing the stochastic acceleration timescale.

In order to offset the unchanged level emission from electrons, we increase the electron injection luminosity from $L_{\rm inj,0,e} = 3.64 \times 10^{42}\,{\rm erg\,s^{-1}}$ to $L_{{\rm inj},e}\,(t = t_0) = 4.9 \times 10^{43}\,{\rm erg\,s^{-1}}$. This has the effect of increasing the electron synchrotron radiation to produce a strong flare in the IR/optical/UV bands. As with the leptonic model light curve analysis of 3C 454.3, we find that it is unnecessary to change the electron spectral index during the peak of the flare. A harder or softer spectral index will worsen the spectral fits during the peak of the flare on the SED. However, changing the proton spectral index is indeed necessary to improve the fits for the harder spectral index from the X-rays to high-energy γ-rays; see Figure 2. Using a common spectral component between the X-rays and high-energy γ-rays and producing a harder index from $q_p = 2.2$ to $q_p(t = t_0) = 1.9$ produces a strong flare in the high-energy γ-ray band with a moderate flare in the X-ray band. The choice of changing the proton spectral index is able to vastly improve the fits of the SED during the flare in comparison to the one-zone leptonic model. For a developing shock that is responsible for a flare, an increased compression ratio can lead to a harder spectral index, which in turn reproduces the harder synchrotron spectra seen in the peak SED of the flare. The proton spectral index and acceleration timescale are adjusted to better improve the quality of the fits to the SED during the peak of the flare.

Due to the change in the acceleration timescale, the protons move to higher energies, but their synchrotron emission produces poor fits to the location of the observed γ-ray peak frequency during the peak of the flare. Therefore, we decreased the background magnetic field from $B = 125\,{\rm G}$ to $B(t = t_0) = 75\,{\rm G}$. A reduced magnetic field can be the result of magnetic reconnection events taking place in the acceleration zone. Lowering the background magnetic field leads to reduced synchrotron cooling, producing even more energetic electrons and protons. The combination of a reduced magnetic field and increased particle acceleration causes the proton synchrotron spectra to peak at $\nu_{\rm obs}^{\rm pk} \approx 1.5 \times 10^{23}\,{\rm Hz}$, consistent with the peak flux levels seen in the SED. Lowering the magnetic field has the added effect of lowering the proton and electron synchrotron flux. The acceleration timescale and electron injection luminosity are adjusted to offset the reduction in the magnetic field until a satisfactory fit is obtained for the flux levels in the broadband SED during the peak of the flare.

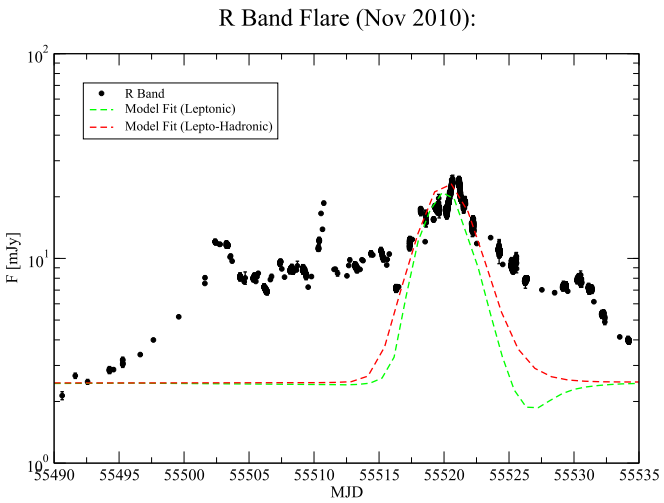

Figure 5. Light curve fit between the data of the 2010 November 19–20 (MJD 55519-55520) flare and the leptonic and lepto-hadronic models in the R band in units of mJy.

With the variations of the magnetic field, acceleration timescale, electron injection luminosity, and proton spectral index (see Table 2), we obtain good fits to the 2010 November flare SED (see Figure 2). A shock scenario that produces a harder proton spectral index produces the spectral fits to the SED of 3C 454.3 in the X-rays and γ-rays during the peak of the 2010 November flare. Increasing the electron injection leads to a prominent flare in the IR/optical/UV bands that is in good agreement with the data. Decreasing both the magnetic field and acceleration timescale produces more energetic protons that reproduce the peak proton synchrotron spectra in the high-energy γ-rays. Based on these flare-state SED fits, we can then integrate the time-dependent fluxes over frequency in the optical R, *Swift* XRT, and *Fermi* γ-ray bands to model the light curves of the flare. The comparison shown in Figures 3–5 is done between model fluxes and the deconvolved measured fluxes; i.e., we have not folded our model spectra through the respective instrument response functions. The light curves in all three bands rise on a timescale of the order of the shock timescale in the observer's frame $t_{\rm rise,obs} \sim \sigma/\delta \approx 1.6 \times 10^5\,{\rm s} \approx 2\,{\rm days}$. As the perturbations subsides, the particles cool in the *Fermi* γ-ray bandpass with a synchrotron cooling timescale in the observer's frame of $t_{\rm cool,obs} \approx 3.5 \times 10^5\,{\rm s} \approx 4\,{\rm days}$, consistent with the decay timescale for the light curve in the *Fermi* bandpass. In our model, we considered both radiative and

adiabatic losses. At the highest energies, protons lose energy due to synchrotron losses, but at lower energies, adiabatic losses dominate. As the acceleration timescale drops below the adiabatic loss timescale in the comoving frame, the lower energy particles are accelerated, producing a flare in the X-ray band. Once the perturbation subsides, the particles then cool on a timescale of the order of the adiabatic loss timescale, $t_{\rm ad,obs} \approx 2.5 \times 10^5$ s ≈ 3 days, in rough agreement with the decay timescale of the light curve in the *Swift* XRT bandpass during the flare. The electrons producing IR/optical/UV radiation cool via synchrotron losses at an extremely fast rate, $t_{\rm cool,obs} \approx (1\text{–}5) \times 10^2$ s. As a result, the optical R band decays on a timescale similar to the shock timescale for the electron injection luminosity, $t_{\rm decay,obs} = \sigma/\delta \approx 1.6 \times 10^5$ s ≈ 2 days.

5. DISCUSSION/CONCLUSIONS

The quiescent state SED of 3C 454.3 can be reproduced by both a one-zone leptonic and a lepto-hadronic model. Both models suggest that the radio to IR/optical/UV emission can be explained by synchrotron emission from electrons/positrons with electron Lorentz factors of $\gamma_e \approx 10^2$–10^3. Because of synchrotron self absorption, radio emission below 10^{12} Hz is strongly self-absorbed in both models. This implies that the observed radio emission must originate from a larger volume further down the jet. For the one zone leptonic model, the high-energy γ-rays can be explained by a combination of external Compton scattering from the accretion disk with a luminosity of $L_d \approx 1.0 \times 10^{46}$ erg s^{-1} and an external radiation field resembling a BLR with a luminosity of $L_{\rm BLR} \approx 2.0 \times 10^{45}$ erg s^{-1}. The combination of the two spectral components is able to reproduce the spectral break observed at 2 GeV, in accordance with previous work performed on 3C 454.3 with one-zone leptonic models (Finke & Dermer 2010; Böttcher et al. 2013). For the one-zone lepto-hadronic model, synchrotron radiation from protons with energies of $E_p \approx 5.0 \times 10^{17}$ eV is responsible for the broadband emission from X-rays to high-energy γ-rays. Our lepto-hadronic model considers synchrotron radiation from secondary particles, such as pions and muons, allowing us to explore larger parameter values of magnetic fields and proton energies in which pion and muon synchrotron can no longer be neglected (Böttcher et al. 2013; Diltz et al. 2015). The fits for the lepto-hadronic model predict the presence of a shoulder in the SED due to muon synchrotron radiation around 20 GeV. Secondary radiation from the electron/positron pairs produced as a result of photo-hadronic interactions is negligible in comparison to muon synchrotron. Pair-dominated high-energy emission in blazars is typically disfavored since such models tend to overproduce the soft X-ray emission due to rapid synchrotron cooling of the electrons/positrons.

In both the leptonic and the lepto-hadronic models, particles are stochastically accelerated due to gyro-resonant interactions with Alfvén waves with a characteristic timescale, $t_{\rm acc}$, given by Equation (3). For both models, the acceleration timescale was left free as an input parameter based on the ratio between the acceleration and escape timescales in the comoving frame. The leptonic model fit suggests that the electrons are efficiently accelerated, $t_{\rm acc}/t_{\rm esc} = 0.1$, while the lepto-hadronic fits requires a much longer acceleration timescale, $t_{\rm acc}/t_{\rm esc} = 4.0$. According to Equation (3), the acceleration timescale is proportional to the dynamical timescale over the size of the region, $l_{\rm dyn}$, in which turbulence is injected, $t_{\rm dyn} = l_{\rm dyn}/c$. Turbulence can be injected on a broad range of size scales. The maximum size represents the size of the emission region. As the turbulence is injected, it cascades onto smaller size scales until reaching the Kolmogrov length scale where viscous dissipation of energy takes place. The size of the injection region describes the size of the eddies that propagate downstream from the onset of turbulence in MHD flows. The quasi-linear approximation assumes that the size of the magnetic field fluctuations is much smaller than the background magnetic field $\xi_i \ll 1$; see Equation (3). Typically, values near $\xi_i \approx 0.1$–0.2 represent the point where the quasi-linear approximation breaks down (Zachary 1987). For both model fits, the Alfvén velocity of the plasma falls in the range $\beta_A \approx 0.4$–0.6, and the escape timescale is $t_{\rm esc} \approx 1.35 \times 10^7$ s. For the quasi-linear approximation to remain valid, the size scales of turbulent eddies that generate Alfvén wave turbulence, may not exceed maximum values of $l_{\rm dyn}^{\rm lep} \approx 6.48 \times 10^{14}$ cm and $l_{\rm dyn}^{\rm had} \approx 5.82 \times 10^{16}$ cm for the leptonic and the lepto-hadronic model, respectively. This corresponds to 2.5×10^{-2} and 2.15 times the size of the emission region for the leptonic and the lepto-hadronic model, respectively. Due to the shorter acceleration timescale for the leptonic model, the turbulence needs to be generated on size scales significantly smaller than the size of the emission region for the quasi-linear approximation to remain valid. For the lepto-hadronic model, the validity of the quasi-linear approximation poses no additional constraint.

Large magnetic fields, $B \approx 100$ G, were necessary to provide adequate fits to the broadband SEDs with our lepto-hadronic model. These large magnetic fields are in accordance with values used in previous proton-synchrotron-dominated hadronic models for FSRQs and BL Lac objects (Böttcher et al. 2013; Cerruti et al. 2015). These large magnetic field estimates are in conflict with recent measurements of radio core shifts of blazars, which argue for magnetic fields on the order of 0.1–1 G at distances of 0.1–1 pc along the jet (Kutkin et al. 2014; Zdziarski et al. 2015). Zdziarski et al. (2015) derived magnetic field estimates based on observed blazar jet opening angles of $\theta = k/\Gamma$, where $k = 0.1$–0.2 (Jorstad et al. 2005; Pushkarev et al. 2009). This approach led to similar magnetic field estimates based on equipartition between the energy densities in the magnetic field and in relativistic electrons, and estimates based on the flux of the partially synchrotron self-absorbed spectrum (Zdziarski et al. 2015). However, jet opening angles corresponding to $k = 1$ yield magnetic field estimates that deviate very strong from equipartition, $\epsilon_{eB} \approx 10^{-9}$. In our model, we considered jet opening angles where $\theta = 1/\Gamma$. To establish values close to equipartition, large values for the proton power, $L_p \approx 7.5 \times 10^{48}$ erg s^{-1}, are needed for the fits, exceeding the Eddington luminosity of the black hole by almost two orders of magnitude. These large values for the proton kinetic luminosity are a common feature in lepto-hadronic models of blazar emission (Böttcher et al. 2013; Cerruti et al. 2015; Petropoulou et al. 2015).

Based on the quiescent state SED fits, we selected a subset of the input parameters to model the prominent flare observed on 2010 November. We consider four parameters: magnetic field, stochastic acceleration timescale, particle injection luminosity, and particle spectral index and modeled them as Gaussian functions in time (see Equations (5)–(8)). We apply

these perturbations to both models in order to determine which model can best explain both the SED of 3C 454.3 in the flare state and the light curves collected in the optical R, *Swift* XRT, and *Fermi* γ-ray bands from the quiescent state SED (Abdo et al. 2010) to the flare-state SED (Wehrle et al. 2012). We found that with the one-zone leptonic model (see Table 2) we are unable to find parameter variations that successfully reproduce the SED in the X-ray and γ-ray bands during the peak of the flare. This is because increased stochastic acceleration (required to model the substantial γ-ray flare) depletes the number of low-energy electrons responsible for the low-energy tails for both the SSC and EC spectral components. Lowering the acceleration efficiency produces too few high-energy electrons to upscatter the external radiation fields to the *Fermi* γ-ray flux levels seen during the 2010 November flare. This result suggests either a temporary increase of the external radiation fields or a scenario that considers static and moving mirrors in the jet as the source of soft photons for upscattering to high-energy γ-rays as a useful alternative to explain the 2010 November flare (Tavani et al. 2015).

With the one zone lepto-hadronic model, we were able to obtain acceptable spectral fits to the entire SED for both the quiescent and the flaring states. Decreasing the spectral index of the proton distribution provides a natural explanation for the harder spectrum between X-rays and high-energy γ-rays seen during the peak of the flare. The model light curves resulting from our proposed flaring scenario provide satisfactory fits to the peaks of the observed optical R, *Swift* XRT, and *Fermi* light curves, starting out from the quiescent state to the flare state (i.e., neglecting the plateau states before and after the flare). We did not attempt to model the enhanced states before the main November 19–20 γ-ray flare since no extensive simultaneous SED data was collected during this time (Wehrle et al. 2012), so any such attempt would have been very poorly constrained.

This work was funded by NASA through Astrophysics Data Analysis Program grant NNX12AE43G. The work of M.B. is supported through the South African Research Chair Initiative of the National Research Foundation[3] and the Department of Science and Technology of South Africa, under SARChI Chair grant No. 64789. This study is partly based on data taken and assembled by the WEBT collaboration and stored in the WEBT archive at the Osservatorio Astronomico di Torino—INAF (http://www.oato.inaf.it/blazars/webt/).

REFERENCES

Abdo, A. A., Ackermann, M., Agudo, I., et al. 2010, ApJ, 716, 30
Abdo, A. A., Ackermann, M., Ajello, M., et al. 2011, ApJ, 733, 26
Ackermann, M., Ajello, M., Baldini, L., et al. 2010, ApJ, 721, 1383
Aharonian, F. A. 2000, NewA, 5, 377
Aharonian, F. A., Atoyan, A. M., & Nagapetyan, A. M. 1983, Ap, 19, 187
Aharonian, F. A., Akhperjanian, A. G., Bazer-Bachi, A. R., et al. 2007, ApJ, 664L, L71
Albert, J., Aliu, E., Anderhub, H., et al. 2007, ApJ, 669, 862A
Asano, K., & Hayashida, M. 2015, ApJ, 808L, 18A
Asano, K., Takahara, F., Toma, K., et al. 2014, ApJ, 780, 64A
Becker, P. A., Le, T., & Dermer, C. D. 2006, ApJ, 647, 539B
Bentz, M. C., Denney, K. D., Grier, C. J., et al. 2013, ApJ, 767, 149B
Blandford, R. D., & Levinson, A. 1995, ApJ, 441, 79
Blazejowski, M., Sikora, M., Moderski, R., & Madejski, G. M. 2000, ApJ, 545, 107B
Bonnoli, G., Ghisellini, G., Foschini, L., Tavecchio, F., & Ghirlanda, G. 2011, MNRAS, 410, 368
Böttcher, M., Harris, D. E., & Krawczynski, H. 2012, Relativistic Jets from Active Galactic Nuclei (New York: Wiley-VCH)
Böttcher, M., Reimer, A., Sweeney, K., & Prakash, A. 2013, ApJ, 768, 54
Cao, G., & Wang, J. 2014, ApJ, 783, 108C
Carasco, L., Carraminana, A., Recillas, E., et al. 2010, ATel, 2988, 1C
Cerruti, M., Zech, A., Boisson, C., & Inoue, S. 2015, MNRAS, 448, 910C
Chen, X., Chatterjee, R., Fossati, G., & Pohl, G. 2013, EPJWC, 6105011C
Collmar, W., Böttcher, M., & Krichbaum, T. P. 2010, A&A, 522, 66C
Dermer, C. D., Cerruti, M., Lott, B., et al. 2014, ApJ, 782, 82D
Dermer, C. D., & Menon, G. 2009, High Energy Radiation from Black Holes: Gamma Rays, Cosmic Rays, and Neutrinos (Princeton, NJ: Princeton Univ. Press)
Dermer, C. D., Miller, J. A., & Li, H. 1996, ApJ, 456, 106D
Dermer, C. D., Murase, K., & Ionue, Y. 2014, JHEAp, 3, 29
Dermer, C. D., & Schlickeiser, R. 1993, ApJ, 416, 458
Dermer, C. D., Schlickeiser, R., & Mastichiadis, A. 1992, A&A, 256, L27
Diltz, C., & Böttcher, M. 2014, JHEAp, 1, 63D
Diltz, C., Böttcher, M., & Giovanni, F. 2015, ApJ, 802, 133D
Finke, J., & Dermer, C. 2010, ApJ, 714L, 303F
Ghisellini, G., Celotti, A., Fossati, G., Maraschi, L., & Comastri, A. 1998, MNRAS, 301, 451G
Giommi, P., Blustin, A. J., Capalbi, M., et al. 2006, A&A, 456, 911
Greco, A., Taktakishvili, A. L., Zimbardo, G., et al. 2002, JGR, 107, 1267
Halzen, F., & Zas, E. 1997, ApJ, 488, 669
Hartman, R. C., Böttcher, M., Aldering, G., et al. 2001, ApJ, 553, 683H
Hoshino, M. 2012, PhRvL, 108, 135003
Hümmer, S., Rüger, M., Spainer, F., & Winter, W. 2010, ApJ, 721, 630H
Jones, F. C. 1968, PhRv, 167, 1159
Jorstad, S. G., Marscher, A. P., Smith, P. S., et al. 2013, ApJ, 773, 147J
Jorstad, S. G., Marscher, A. P., Lister, M. L., et al. 2005, AJ, 130, 1418J
Joshi, M., & Böttcher, M. 2011, ApJ, 727, 21J
Kelner, S. R., & Aharonian, F. A. 2008, PhRvD, 78, 034013
Kistler, M. D., Stanev, T., & Yüksel, H. 2014, PhRvD, 90, 123006
Kutkin, A. M., Sokolovsky, K. V., Lisakov, M. M., et al. 2014, MNRAS, 437, 3396K
Lazarian, A., & Vishniac, E. T. 1999, ApJ, 517, 700
Lazarian, A., Vlahos, L., Kowal, G., et al. 2012, SSRv, 173, 557
Mannheim, K. 1993, A&A, 269, 69
Mannheim, K., & Biermann, P. L. 1992, A&A, 253, L21
Mastichiadis, A., & Kirk, J. G. 1995, A&A, 295, 613
Mastichiadis, A., & Kirk, J. G. 2005, A&A, 433, 765
Matthaeus, W. H., & Lamkin, S. L. 1986, PhFl, 29, 2513
Mücke, A., & Protheroe, R. J. 2001, APh, 15, 121
Mücke, A., Protheroe, R. J., Engel, R., Rachen, J. P., & Stanev, T. 2003, APh, 18, 593
Murase, K., Inoue, Y., & Dermer, C. D. 2014, PhRvD, 90, 023007
Padovani, P., Petropoulou, M., Giommi, P., & Resconi, E. 2015, MNRAS, 452, 1877
Pennanen, T., Vrum, I., & Poutanen, J. 2014, A&A, 564A, 77
Petropoulou, M., Dimitrakoudis, S., Padovani, P., et al. 2015, MNRAS, 448, 2412
Pian, E., Foschini, L., Beckmann, V., et al. 2006, A&A, 449, L21
Pushkarev, A. B., Kovalev, Y. Y., Lister, M. L., & Savolainen, T. 2009, A&A, 507, L33
Raiteri, C. M., Villata, M., Aller, M. F., et al. 2011, A&A, 534, 87
Saito, S., Stawarz, L., Tanaka, T., et al. 2015, ApJ, 809, 171S
Sanchez, S., & Escande, L. 2010, ATel, 3041, 1S
Schlickeiser, R. 1984, A&A, 136, 227
Schlickeiser, R. 1996, A&AS, 120, 481
Shakura, N. I., & Sunyaev, R. A. 1973, A&A, 24, 337
Sikora, M., Begelman, M., & Rees, M. 1994, ApJ, 421, 153
Sironi, L., & Spitkovski, A. 2014, ApJ, 783L, 21S
Sol, H., Zech, A., Boisson, C., et al. 2013, APh, 43, 215S
Striani, E., Lucarelli, F., Vercellone, S., et al. 2010, ATel, 3034, 1S
Tavani, M., Vittorini, V., & Cavaliere, A. 2015, ApJ, 814, 51T
Urry, C. M. 1998, AdSpR, 21, 89
Veltri, P., Zimbardo, G., Taktakishvili, A. L., & Zelenyi, L. M. 1998, JGR, 103, 14
Vercellone, S., Chen, A. W., Giuliani, A., et al. 2008, ApJL, 676L, 13V
Vercellone, S., Striani, E., Vittorini, V., et al. 2011, ApJ, 736L, 38V
Villata, M., Raiteri, C. M., Balonek, T. J., et al. 2006, A&A, 453, 817V

[3] Any opinion, finding, and conclusion or recommendation expressed in this material is that of the authors and the NRF does not accept any liability in this regard.

Villata, M., Raiteri, C. M., Aller, M. F., et al. 2007, A&A, 464, 5V
Vittorini, V., Tavani, M., Cavaliere, A., Striani, E., & Vercellone, S. 2014, ApJ, 793, 98V
Wehrle, A. E., Marchser, A. P., Jorstad, S. G., et al. 2012, ApJ, 758, 72W
Weidinger, M., & Spanier, F. 2015, A&A, 573, A7
Yan, D., & Zhang, L. 2014, MNRAS, 447, 2810Y
Yokoi, N., Higashimori, K., & Hoshino, M. 2013, PhPl, 20, 12
Zachary, A. 1987, PhD Dissertation, Univ. California
Zdziarski, A. A., Sikora, M., Pjanka, P., & Tchekhovskoy, A. 2015, MNRAS, 451, 927Z
Zhang, H., & Böttcher, M. 2013, ApJ, 774, 18
Zhang, H., Chen, X., & Böttcher, M. 2014, ApJ, 789, 66Z